



1 **Measurement Report: Development of a portable peroxy
2 radical measurement system and application for diagnosing
3 local ozone formation and transport**

4 Rujia Tang^{1,2#}, Zelong Zheng^{1,2#}, Yiming Wang^{1,2}, Hongxia Liu^{1,2}, Xiaorui Chen^{1,2*},
5 Haichao Wang^{1,2}

6 1 School of Atmospheric Sciences, Sun Yat-sen University, Southern Marine Science
7 and Engineering Guangdong Laboratory (Zhuhai), Zhuhai, 519082, China

8 2 Guangdong Provincial Observation and Research Station for Climate Environment
9 and Air Quality Change in the Pearl River Estuary, Key Laboratory of Tropical
10 Atmosphere-Ocean System, Ministry of Education, Zhuhai, 519082, China

11 # These authors contributed equally to this work

12 *Correspondence: X.R.C. (chenxr95@mail.sysu.edu.cn)*

13

14 **Abstract**

15 Atmospheric total peroxy radicals RO_2^* ($\text{RO}_2^* = \text{HO}_2 + \text{RO}_2$) play central roles
16 in tropospheric chemistry, governing the formation of ozone and secondary aerosols.
17 However, due to their extremely low concentrations and high reactivity, direct
18 observation of RO_2^* remains challenging. In this study, a compact instrument for in-
19 situ measurement of RO_2^* was developed by combining the Peroxy Radical Chemical
20 Amplification (PERCA) technique with Cavity-Enhanced Absorption Spectroscopy
21 (CEAS). By optimizing operational parameters, the system can achieve a chemical
22 chain length of 56 and an optimal detection limit of 0.2 pptv (1σ , 3 min), enabling
23 highly sensitive measurements of ambient peroxy radicals. The self-constructed
24 PERCA-CEAS system was successfully deployed in a field campaign during autumn
25 in Zhuhai to observe ambient RO_2^* . During the observation period, the mean daytime
26 RO_2^* was 31.11 ± 18.87 pptv, which resulted in an average of 14.41 ± 17.04 ppbv/h
27 $\text{P}(\text{O}_3)$. The comparison of O_3 variation and derived $\text{P}(\text{O}_3)$ indicates that the daytime
28 ozone enhancement in Zhuhai was primarily driven by local photochemical production,
29 while regional transport acted mainly as an export effect. Our results demonstrate that



30 a compact PERCA-CEAS system is capable of ambient RO₂* measurements and
31 suggest the need of diagnosing O₃ formation pattern with the constraint of high time-
32 resolution RO₂* concentration.

33 **Short Summary**

34 This study developed a portable measurement system based on cavity-enhanced
35 absorption spectroscopy, enabling highly sensitive online monitoring of total peroxy
36 radicals in the atmosphere. The system is compact and was successfully deployed in a
37 field campaign in Zhuhai during autumn. The results indicate that daytime ozone
38 enhancement in this region was primarily driven by local photochemical production,
39 while regional transport mainly played an export role.

40



41 1. Introduction

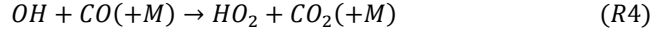
42 In the troposphere, total peroxy radicals RO_2^* ($\text{RO}_2^* = \text{HO}_2 + \text{RO}_2$) are key
43 reactive species that drive photochemical reaction chains in the atmosphere (Monks,
44 2005). The production and recycling of RO_2^* determine both the persistence and
45 efficiency of photochemical reactions. The continual regeneration of NO_2 through
46 radical- NO_x chain reactions sustains ozone production and leads to its accumulation
47 (Orlando and Tyndall, 2012; Wang et al., 2022). Moreover, the removal of RO_2^* also
48 contribute to the formation of secondary organic aerosols (Chen et al., 2022; Ehn et al.,
49 2014; Zou et al., 2025), which plays a crucial role in regional air quality and climate
50 impacts (Liang et al., 2024). Therefore, understanding the spatiotemporal variations of
51 RO_2^* is essential for elucidating the evolution of regional atmospheric oxidation
52 capacity and assessing pollution formation potential.

53 Significant advancements have been made in atmospheric peroxy radical
54 measurement techniques over the past few decades, primarily categorized into two
55 technological pathways: direct and indirect measurements (Gao et al., 2023). The
56 microwave-induced electron spin resonance (MIESR) method identifies radicals
57 through the resonance of unpaired electrons, providing the most direct evidence of their
58 detection. However, MIESR suffers from low sensitivity and complex operation
59 requirements (Mihelcic et al., 1985, 1990). Indirect measurement techniques detect
60 RO_2^* by converting it into measurable species through chemical reactions. For example,
61 the Laser-Induced Fluorescence (LIF) technique determines RO_2^* concentrations by
62 measuring the OH fluorescence signal generated from the reaction between RO_2^* and
63 NO. This method offers high sensitivity and selectivity, whereas requires a complex
64 setup and is prone to environmental interferences (Lu et al., 2012; Whalley et al., 2013).
65 The Peroxy Radical Chemical Ionization Mass Spectrometry (PerCIMS) method
66 converts RO_2^* into characteristic ions through ion-molecule reactions, enabling highly
67 sensitive and selective quantification of specific radicals (Edwards et al., 2003;
68 Hornbrook et al., 2011). Unlike other approach, the peroxy Radical Chemical
69 Amplification (PERCA) measures RO_2^* by amplifying its signal into a large amount of
70 NO_2 through a chain reaction. The PERCA system has relatively high sensitivity to
71 atmospheric RO_2 radicals. The simple construction and routine maintenance for this



72 system ensure the stable measurement on the field. As a result, PERCA has been widely
73 employed in atmospheric observations (George et al., 2020; Liu and Zhang, 2014; Wei
74 et al., 2023).

75 In the PERCA system, NO and CO gases are introduced to trigger a series of chain
76 reactions to convert minor peroxy radicals into detectable NO₂. When sampled air
77 enters the reactor, RO₂ reacts with NO to produce HO₂ and NO₂ (R1, R2). The HO₂
78 then reacts with excess NO to generate OH and NO₂ (R3), and the OH reacts with CO
79 to recycle back to HO₂ (R4). Through this chain reaction cycle, the low-concentration
80 peroxy radical signal is progressively amplified into a high-concentration NO₂ signal
81 (Cantrell et al., 1996). The chemical chain length (CL), defined as the average number
82 of radical propagation cycles occurring within the reactor, serves as a quantitative
83 indicator of the amplification efficiency. The magnitude of CL is governed by the
84 competing rates of radical propagation, termination reactions, and physical losses inside
85 the reactor (Kartal et al., 2010; Reichert et al., 2003). Once the amplified NO₂
86 concentration (Δ NO₂) is determined, the concentration of RO₂* in ambient air can be
87 derived using the calibrated CL value according to Eq. (1).



$$[RO_2^*] = \frac{\Delta[NO_2]}{CL} \quad (Eq. 1)$$

93 Significant progress has been made in peroxy radical chemistry observations and
94 modeling studies in China in recent years. However, most field measurements have
95 been conducted in the major city clusters, such as North China Plain (Ma et al., 2019;
96 Tan et al., 2017, 2018b), the Yangtze River Delta (Lou et al., 2022; Ma et al., 2022),
97 and the Pearl River Delta (Lu et al., 2012; Tan et al., 2019; Yang et al., 2022), while
98 other regions remain underexplored. In addition, RO₂* studies have primarily focused
99 on the urban and inland areas, with limited exploration within the coastal boundary
100 layer (Zhang et al., 2023). The lack of peroxy radical measurements would also
101 constrain direct assessment of photochemical ozone production. In-situ measurements
102 of ambient RO₂* provide a direct basis for calculating local P(O₃), as previous studies
103 have demonstrated that observed peroxy radical concentrations enable quantitative



104 assessment of instantaneous ozone production rates and its related chemistry across
105 diverse chemical environments (Sommariva et al., 2010; Thornton et al., 2002).
106 Furthermore, the calculated local $P(O_3)$ combined with the observed O_3 variation
107 provides a powerful means to quantify the contribution of ozone transport (Tan et al.,
108 2021). Therefore, developing portable and high-time-resolution RO_2^* measurement
109 techniques and applying them to diverse atmospheric environments are crucial for
110 advancing our understanding of complex photochemical processes in the troposphere.

111 In recent years, optical techniques such as Cavity Enhanced Absorption
112 Spectroscopy (CEAS) have developed rapidly. In our previous work, we constructed a
113 compact and lightweight CEAS instrument with high temporal and spatial resolution
114 for precise NO_2 measurements (Zheng et al., 2024). Building upon this foundation, the
115 current study integrates CEAS with the PERCA system, enabling portable and stable
116 detection of ambient RO_2^* measurements. We utilized this system to conduct
117 observations of RO_2^* concentration levels in coastal area during the autumn. Based on
118 our measurements, the local photochemical $P(O_3)$ was derived and subsequently
119 applied to analyzing the influence of transport on O_3 under both clean and polluted
120 conditions.

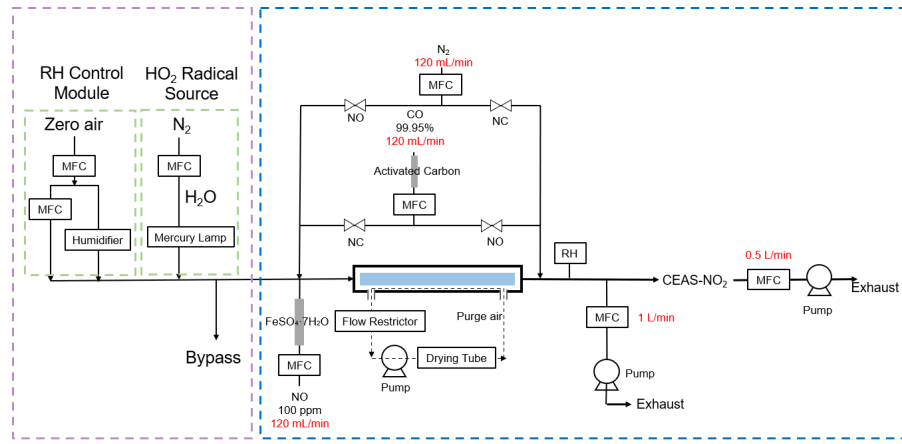
121

122 **2. Experiment and methods**

123 The design of our instrument emphasizes a balance between detection
124 performance (e.g. sensitivity and accuracy) and portability in the field. The PERCA-
125 CEAS system consists of two major components: a chemical amplification module and
126 an NO_2 detection module. The former converts trace radicals into detectable NO_2
127 signals, while the latter provides precise quantification of the generated NO_2 . The
128 chemical amplification module adopts a single-channel configuration to reduce system
129 complexity and physical size while maintaining measurement accuracy. Although
130 conventional dual-channel PERCA systems can effectively remove background
131 interferences, they require two NO_2 detectors operating in parallel (Chen et al., 2016;
132 Liu and Zhang, 2014), leading to potential discrepancy resulted from optical parameters
133 and flow between two channels. In contrast, the single-channel design offers better
134 structural compactness and operational stability. The produced NO_2 concentration is



135 measured by a self-built CEAS system, which features compact size (40 cm × 30 cm ×
136 17 cm) and lightweight design (5.80 kg). Detailed information of CEAS is provided in
137 our previous work (Zheng et al., 2024). The overall structure of the PERCA-CEAS
138 system is presented in Figure. 1.



139
140 Figure 1. Schematic diagram of the PERCA-CEAS system. The purple dash line portion represents
141 the standard source module, which consists of the standard gas generation unit and the relative
142 humidity (RH) control unit (outlined in green) and is used for calibrating the system chain length.
143 The blue dash line portion represents the measurement module, comprising the chemical
144 amplification unit and the NO₂ detection unit, which together enable the quantification of
145 atmospheric peroxy radicals.
146

147 2.1 Chemical amplification module

148 We use NO (8 ppmv) and CO (8 %) gases as reactants accompanied by N₂ as a
149 balancing gas. To ensure gas purity, a series of purification steps were applied before
150 the gases entered the reaction chamber. NO was passed through a ferrous sulfate
151 heptahydrate (FeSO₄·7H₂O) filter to remove trace NO₂ by reduction, while CO was
152 purified with an activated carbon column to eliminate residual carbonyl compounds
153 from the gas cylinder. To accommodate the single-channel configuration, an automatic
154 mode-switching module was designed to switch between amplification and background
155 modes. In this setup, NO is continuously introduced from the front of the reaction tube,
156 while both N₂ and CO flows were divided into two branches through a three-way
157 solenoid valve before entering the system. During the amplification mode, NO and CO
158 are introduced from the front end and N₂ from the rear; during the background mode,
159 NO and N₂ enter from the front while CO is fed from the rear. A programmable timer



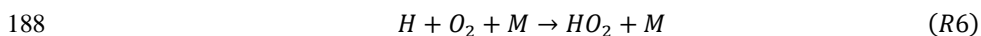
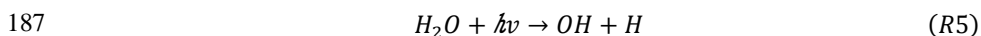
160 controls the opening and closing of these four solenoid valves, allowing timed
161 switching between the two modes and enabling real-time online detection of peroxy
162 radicals.

163 Humidity plays a critical role in determining the efficiency of chemical
164 amplification reactions. To control water vapor levels, a Nafion tube dryer (model MD-
165 700-12-F-3, total length 40 cm, effective length 30 cm) was used to remove water vapor
166 and serve as the chemical amplification reaction place in the meantime. To ensure
167 efficient drying and maintain a low-humidity sample stream, a continuous flow of dry
168 purge gas was introduced along the outer side of the Nafion tube. In this work, the dry
169 purge gas was generated by a pump-driven system connected in series with a drying
170 tube filled with indicating silica gel. The gas was first deeply dried through the silica
171 gel column to ensure extremely low moisture content before being circulated from the
172 lower inlet to the upper outlet of the Nafion tube, forming a closed-loop flow. A
173 humidity sensor was installed at the outlet of the sample stream to continuously monitor
174 the relative humidity inside the reaction tube. Through this precise humidity control,
175 the relative humidity on the chemical amplification process was maintained under 20%,
176 ensuring system stability and improving the reliability of the experimental results.

177

178 2.2 Chain length calibration

179 As described in the principle of the chemical amplification method (Eq. (1)), the
180 CL is a key parameter determining the accuracy of peroxy radical measurements.
181 Therefore, the CL of this instrument must be calibrated using a standard peroxy radical
182 source. Calibration is performed with radicals generated on-site. In this study, a HO_2
183 radical source was generated by photolysis of H_2O using a pen-shaped mercury lamp.
184 Under UV irradiation, H_2O is photolyzed to produce OH and H (R5). The generated H
185 radical can rapidly combine one O_2 to form the hydroperoxyl radical HO_2 through
186 reaction (R6).



189 To calibrate the PERCA system, we used the four NO_2 signals detected by the
190 CEAS as calibration references. The calibration procedure comprises four steps as



191 follows. Firstly, when the mercury lamp was turned on, H_2O was photolyzed under UV
192 irradiation to generate the HO_2 source. NO and CO were introduced into the upper inlet
193 of the reaction cell, while N_2 was introduced from the lower inlet. The measured signal,
194 S_1 , represents the NO_2 concentration after radical chemical amplification. Secondly,
195 when NO and N_2 were introduced into the upper inlet and CO into the lower inlet, the
196 signal S_2 represents the NO_2 concentration under the radical-background mode. Thirdly,
197 the mercury lamp was turned off, and the HO_2 is removed. With NO and CO introduced
198 into the upper inlet and N_2 into the lower inlet, the signal S_3 represents the NO_2
199 concentration under the chemical amplification mode without radicals. When NO and
200 N_2 were introduced into the upper inlet and CO into the lower inlet, the signal S_4
201 corresponds to the NO_2 concentration under the background mode without radicals.
202 Based on above measured NO_2 signals (S_1 , S_2 , S_3 and S_4), the CL can be calculated
203 using Eq. (2). Here, $S_2 - S_4$ represents the NO_2 signal difference produced by the peroxy
204 radicals generated from the standard source under the background mode, reflecting their
205 original concentration level. The $S_1 - S_3$ corresponds to the total NO_2 signal difference
206 obtained under the chemical amplification mode, where the same amount of peroxy
207 radicals is amplified through the reaction cycles. Therefore, the CL can be determined
208 from the ratio of ($S_1 - S_3$) to ($S_2 - S_4$).

$$209 \quad CL = \frac{\Delta \text{NO}_2}{[\text{HO}_2]} = \frac{S_1 - S_3}{S_2 - S_4} \quad (\text{Eq. 2})$$

210

211 3. Results and discussion

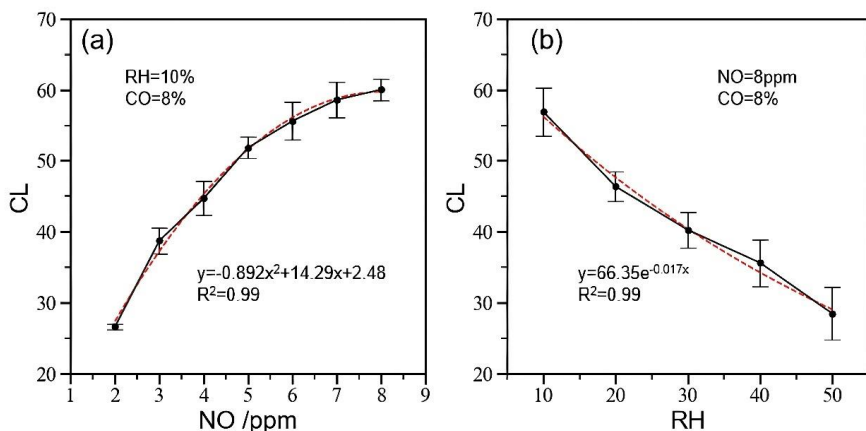
212 3.1 Dependence of the CL on Reaction Conditions

213 The CL is influenced by several factors, including the concentrations of reactive
214 gases, reaction time, relative humidity, and wall losses (Liu and Zhang, 2014). To
215 investigate the response of CL to these parameters in our PERCA-CEAS system, we
216 measured the CL under a series of controlled conditions, specifically by varying NO
217 concentrations and RH levels. The CL measurement was repeated at least five time for
218 each condition. For the subsequent experiments, the CO concentration was fixed at 8%,
219 which is sufficiently high to sustain efficient HO_2 production while remaining within
220 safe limits of CO (explosion range: 12.5–74.2%).



221 To assess how NO concentration influences CL, we conducted a series of
222 experiments under varying NO levels while keeping the relative humidity fixed at 10%.
223 As shown in Figure 2(a), CL increases steadily with increasing NO concentration and
224 reaches its maximum when NO is 8 ppm. Considering both measurement efficiency
225 and system economy, 8 ppm was chosen as the optimal NO concentration for instrument
226 operation.

227 At high RH, water vapor on the reactor walls enhances the heterogeneous uptake
228 of RO_2 and HO_2 and promotes HOx-terminating reactions, thereby suppressing chain
229 propagation and shortening the CL (Mihele et al., 1999; Yang et al., 2019) . To quantify
230 the effect of RH on the CL, a custom-built humidifier was used to control the flow rate
231 of the humidified gas, thereby generating HO_2 sources at different RH levels (10%–
232 50%). The relative humidity of the sample gas was monitored by a temperature–
233 humidity sensor installed downstream of the Nafion reaction tube. The experimental
234 results, presented in Figure 2(b), demonstrate a substantial decrease in CL as the RH
235 increases. Specifically, when the relative humidity (RH) of the sample gas passing
236 through the Nafion dryer reaches 50%, the chain length drops by more than 66%, a
237 reduction that severely compromises the sensitivity required for accurate field RO_2^*
238 measurements. Consequently, to ensure optimal measurement performance, the RH of
239 the airflow entering the amplification zone is strictly controlled to remain below 20%
240 during field campaigns, corresponding to 45% RH in ambient air.



241
242 Figure 2. (a) Relationship between the CL and NO concentration under conditions of 10% RH and
243 8% CO concentration. (b) Variation of CL with RH at a fixed NO concentration of 8 ppm and CO



244 concentration of 8%. (Error bars represent the standard deviation of five independent measurements.)
245

246 The optimal CL for the PERCA-CEAS measurement system (under RH=10%,
247 NO=8ppm, CO=8%) was determined to be 56 ± 4 . Some previous studies have reported
248 much higher CL: for example, (Green et al., 2003) reported $CL \approx 260$ for a single-
249 channel ground system, and (Wood and Charest, 2014) found $CL = 208 \pm 25$ under
250 idealized laboratory conditions (at 0% RH). In comparison, the chain length determined
251 in our study remains consistent with values obtained from PERCA systems that employ
252 similar CRDS or CEAS system, where effective CL commonly fall within the range of
253 44–91 (Duncianu et al., 2020; George et al., 2020; Horstjann et al., 2014). Overall, these
254 results indicate that the CL of our PERCA–CEAS system is reasonable and provides
255 sufficient sensitivity for atmospheric RO_2^* measurements.

256

257 3.2 Detection Limit and Measurement Uncertainty

258 In the PERCA–CEAS system, the concentration of RO_2^* is determined by
259 converting it into measurable NO_2 through chain reactions with excess NO.
260 Consequently, the overall detection limit of the system depends on both the detection
261 limit of NO_2 and the CL, as described by Eq. (3). The LOD for the CEAS- NO_2 model
262 was determined under laboratory conditions by continuously measuring high-purity
263 zero-air for over 5 hours and calculating the standard deviation of blank noise (Zheng
264 et al., 2024) . At a 3 min time resolution, the LOD of NO_2 was determined to be 11.4
265 pptv, which yield a detection limit of 0.2 pptv (1σ , 3min) for RO_2^* .

266 The overall measurement uncertainty of the system was quantified using the
267 Gaussian error propagation (Eq. (4)). Three major sources contribute to the total
268 uncertainty: (1) NO_2 measurement uncertainty (6%), which includes uncertainties in
269 the absorption cross-section (4%), mirror reflectivity calibration (5%), effective cavity
270 length (0.5%), and pressure measurement (0.1%); (2) CL calibration uncertainty (7%),
271 derived from repeated calibration results (56 ± 4); and (3) uncertainty in radical
272 partitioning (8–14%) (Kartal et al., 2010). Based on these factors, the overall
273 uncertainty in ROx measurement was estimated to be 12–17%, demonstrating the
274 robustness and reliability of the PERCA–CEAS system for RO_2^* measurement.



275
$$DL(RO_2^*) = \frac{DL(NO_2)}{CL} \quad (3)$$

276
$$\sqrt{\frac{\sigma_{RO_2^*}}{RO_2^*}} = \sqrt{\left(\frac{\sigma_{NO_2}}{NO_2}\right)^2 + \left(\frac{\sigma_{CL}}{CL}\right)^2 + \left(\frac{\sigma_{Part}}{Part}\right)^2} \quad (4)$$

277

278 3.3 Field Observation of RO₂*

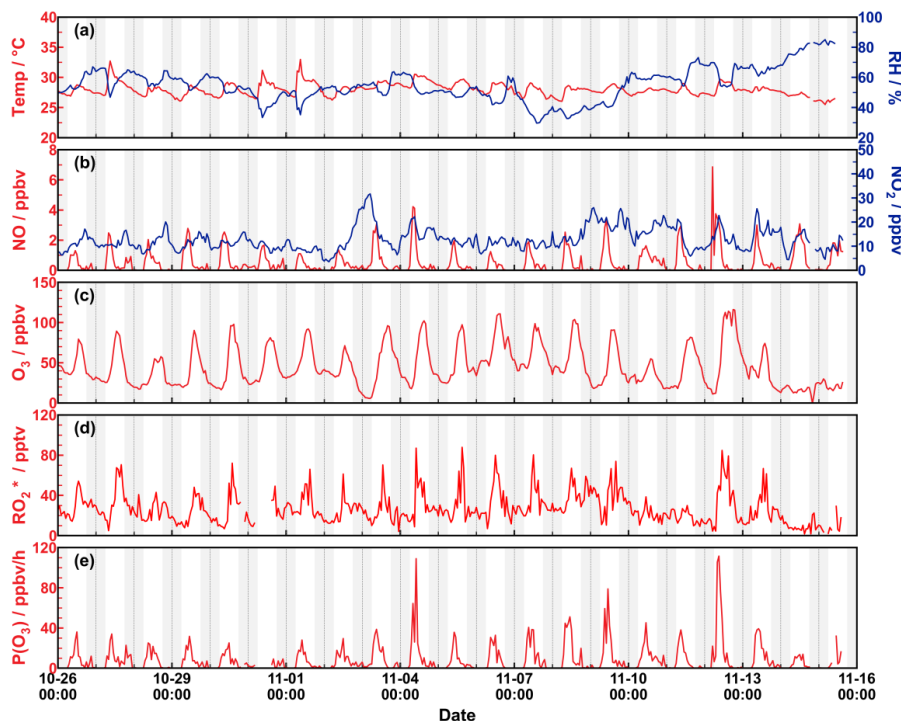
279 The instrument has been deployed in a field campaign to evaluate the performance
280 of instrument under real atmosphere conditions. All instruments are placed on the roof
281 of a six-story building in the campus of Sun Yat-sen University (22° 21' 06" N, 113°
282 35' 42" E), which is located in the western shore of the Pearl River Estuary and
283 approximately 15 km from downtown Zhuhai. The observation site mainly received an
284 airmass mixed with vehicle emissions from a traffic artery (~300m) and nearby
285 residential areas. There are no major industrial facilities in the surroundings.

286 The field observation campaign was conducted from October 26 to November 15,
287 2024, producing more than 15 days of valid continuous RO₂* radical data. For PERCA-
288 CEAS operation, both the chemical amplification mode and the background mode were
289 set to 90 s in this observation, resulting in a time resolution of 3 min. Ambient
290 temperature and relative humidity were continuously monitored using a temperature–
291 humidity probe (HC2A-SH, ROTRONIC, Switzerland). The concentrations of NO and
292 NO₂ were measured by a commercial chemiluminescence analyzer (42i-TL, Thermo,
293 USA), while O₃ concentrations were obtained using a UV photometric analyzer (Model
294 49i, Thermo, USA). The mirror reflectivity of the CEAS detector was calibrated before
295 and after the campaign, and the results remained consistent.

296 Figure 3(a-c) presents the time series of meteorological parameters and major
297 pollutants during the observation period. Ambient temperature was consistently above
298 25 °C, with an average value of 28.44 ± 1.5 °C. Due to the coastal meteorological
299 conditions, the RH was relatively high and show clear diurnal variations—lower during
300 the day and higher at night—ranging from 25% to 85%, with an average of 55.98 ±
301 12.53%. Low NO and NO₂ concentrations were observed with an average of 0.34 ±
302 0.81 ppbv and 13.21 ± 4.72 ppbv, respectively, indicating generally weak NO_x
303 emissions from traffic at this site. The daily maximum of O₃ concentrations ranged from
304 116 to 5.6 ppbv with an average of 44.86 ± 25.03 ppbv, suggesting a moderate level of



305 photochemical pollution during the observation period.



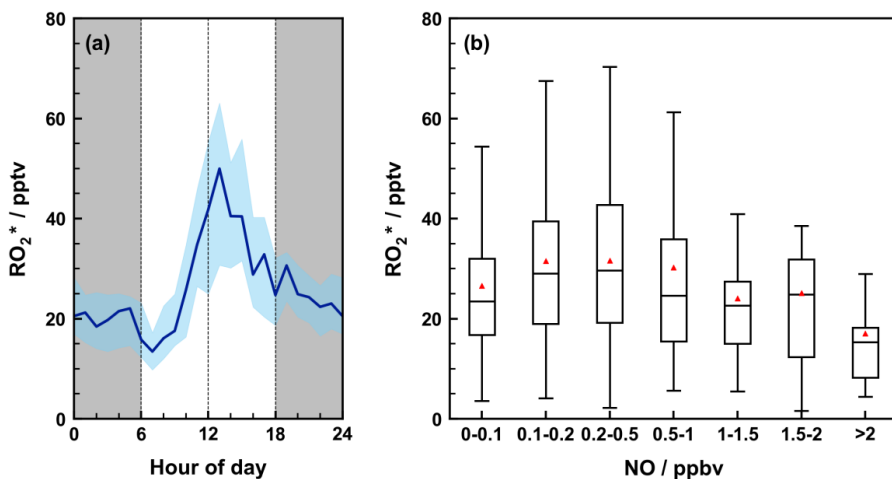
306
307 Figure 3. Time series of meteorological parameters (T, RH), major pollutants (O₃, NO_x, RO₂^{*}), and
308 P(O₃) during the autumn observation period of 2024, with a temporal resolution of 1 hour.
309

310 Compared to previous observation in PRD region, moderate levels of RO₂^{*} were
311 observed with the daily peaks ranging from 48 to 87 pptv (Figure 3d). The RO₂^{*}
312 exhibited a pronounced daytime peak, with an average of 51.3 pptv at around 13:00,
313 and decreased to around 20 pptv at night (Figure 4a). The relatively high level of RO₂^{*}
314 at night indicates the presence of a nighttime peroxy radical source possibly due to NO₃
315 chemistry oxidation, which can be evidenced by the occasional increase of RO₂^{*} after
316 sunset. The daytime average of RO₂^{*} (31.11 pptv) was 1-3 times higher than those
317 reported in most suburban areas, while was lower than those observed in urban areas
318 (Tan et al., 2019; Wang et al., 2023).

319 In addition, our observed RO₂^{*} exhibited nonlinear response to NO variation
320 (Figure 4b). At low NO levels, RO₂^{*} increases with NO by promoting the RO₂^{*}-HOx
321 propagation cycle. Once NO exceeds about 1 ppbv, the excess NO rapidly converts
322 peroxy radicals into termination products (e.g. organic nitrates), thus interrupting the



323 radical chain cycle and leading to a decline in RO₂* concentrations (Thornton et al.,
324 2002). The turning point of NO response is higher than that reported in previous
325 studies(Ma et al., 2022; Wei et al., 2023; Yang et al., 2022). High turning point could
326 be attributed to elevated VOCs reactivity due to distinct VOC components supporting
327 more rapid RO₂* production at this coastal site.



328
329 Figure 4. Diurnal variation of RO₂* and its dependence on NO concentration. (a) Average diurnal
330 variation of RO₂* during the observation period. The gray shaded areas indicate nighttime (18:00–
331 06:00), the dark line represents the median values, and the light blue shading shows the interquartile
332 range (25th–75th percentile). (b) Boxplots of RO₂* distributions under different NO concentration
333 ranges. The black line inside each box denotes the median, and the red triangles indicate the mean
334 RO₂* values for each NO interval.

335

336 3.4 Local production and Transport of Ozone

337 The instantaneous ozone production rate is driven by peroxy radical chain
338 propagation involving the reaction of NO and RO₂* (Griffith et al., 2016) . Therefore,
339 we calculated P(O₃) based on measured RO₂* using Eq. 5. Since the rate constants of
340 HO₂ + NO and RO₂ + NO reactions are similar (the difference between k_{NO+HO2} and k_i
341 is less than 10%) (Orlando and Tyndall, 2012), an effective rate constant k_{eff} is adopted
342 for the calculation, which is typically approximated by the value of k_{NO+HO2} (Anderson
343 et al., 2019). The photochemical loss of ozone D(O₃) is calculated using Eq. 6, including
344 the photolysis, reactions with OH and HO₂, and the reaction of NO₂ with OH (Tan et
345 al., 2021). Here, D(O₃) was derived using kinetic rate constants together with observed
346 mean concentrations (and representative literature values for unmeasured species)



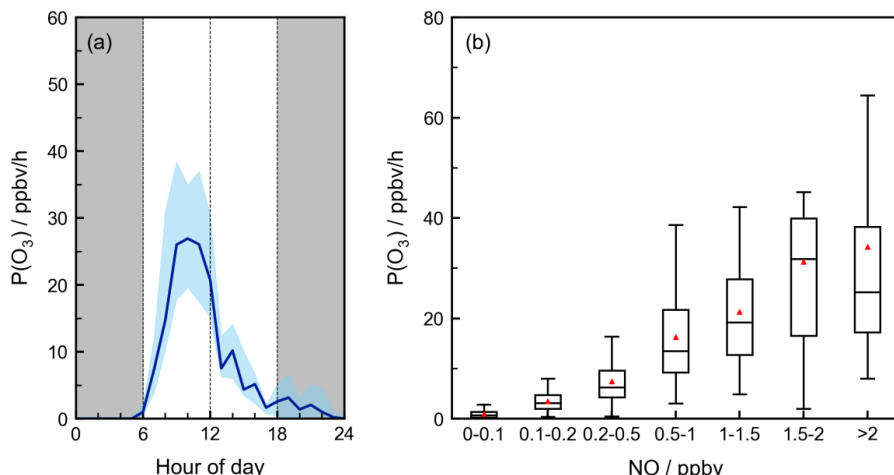
347 under 298 K and 1 atm. Using the typical conditions ($j(O^1D)=1.0\times10^{-5}\text{ s}^{-1}$, $OH=1.0\times10^6$
 348 cm^{-3} , $\text{NO}=10\text{ ppbv}$, $\text{O}_3=40\text{ ppbv}$, $\text{HO}_2\approx15\text{ pptv}$), $D(\text{O}_3)$ was estimated to be $\sim0.70\text{ ppbv}$
 349 h^{-1} , accounting for only $\sim5\%$ of $P(\text{O}_3)$. Therefore, $P(\text{O}_3)$ can be approximated as $P(\text{O}_3)_{\text{net}}$.

$$350 \quad P(\text{O}_3) = k_{\text{NO}+\text{HO}_2}[\text{HO}_2][\text{NO}] + [\text{NO}] \sum_i k_i[\text{RO}_2]_i = k_{\text{eff}}[\text{RO}_2^*][\text{NO}] \quad (\text{Eq. 5})$$

$$351 \quad D(\text{O}_3) = f_{\text{H}_2\text{O}}(O^1D)[\text{O}_3] + k_{\text{OH}+\text{O}_3}[\text{OH}][\text{O}_3] + k_{\text{HO}_2+\text{O}_3}[\text{HO}_2][\text{O}_3] + k_{\text{O}_2+\text{NO}_2}[\text{O}_2][\text{NO}_2] \quad (\text{Eq. 6})$$

$$352 \quad P(\text{O}_3)_{\text{net}} = P(\text{O}_3) - D(\text{O}_3) \quad (\text{Eq. 7})$$

353 Substantial variability in $P(\text{O}_3)$ was observed during the campaign, with daily peak
 354 values ranging from 11 to 110 $\text{ppbv}\cdot\text{h}^{-1}$ and a daytime average of $14.41 \pm 17.04\text{ ppbv}\cdot\text{h}^{-1}$
 355 (Figure. 3e). After sunrise, with increasing solar intensity and NO concentrations,
 356 photochemical reactions became more active, leading to a rapid increase in $P(\text{O}_3)$,
 357 which peaked around 10:00 ($\sim27\text{ ppbv}\cdot\text{h}^{-1}$) (Figure. 5a). Subsequently, $P(\text{O}_3)$ gradually
 358 decreased in the afternoon with the weakening solar radiation. We found a sustaining
 359 increase of $P(\text{O}_3)$ with NO concentration (Figure. 5b), suggesting that ozone formation
 360 fell within the NOx-limited regime under typical daytime conditions at this site. Similar
 361 positive $P(\text{O}_3)$ -NOx relationships have been reported in both urban and suburban
 362 environments — such as the Nashville plume study (Thornton et al., 2002), rural North
 363 China field campaigns (Tan et al., 2018a), and recent observations in Hefei (Yu et al.,
 364 2023). The consistent increase of $P(\text{O}_3)$ and RO_2^* within low NOx levels demonstrate
 365 that the chain propagation for peroxy formation can be enhanced by NO increase and
 366 jointly accelerate instantaneous $P(\text{O}_3)$.



367
 368 Figure 5. Diurnal variation and NO-dependent distribution of $P(\text{O}_3)$. (a) Average diurnal profile of



369 $P(O_3)$ during the observation period. The gray shaded area represents nighttime (18:00–06:00). The
370 dark line denotes the median, and the light blue shading indicates the interquartile range (25th–75th
371 percentile). (b) Box plots of $P(O_3)$ under different NO concentration ranges. The black line inside
372 each box represents the median, and the red triangle marks the mean value within each interval.
373

374 We summarized previously reported observations of RO_2^* , $P(O_3)$, and related
375 parameters in Table 1. The $P(O_3)$ observed in this study was generally higher than those
376 at low-NO sites such as Wangdu (10.44 ppbv·h⁻¹), San Antonio (4.2 ppbv·h⁻¹), and
377 Hefei (5.91 ppbv·h⁻¹) except for a suburban site in northern China (19.5 ppbv·h⁻¹). Even
378 high-NO sites like Paris (15.8 ppbv·h⁻¹) and Heshan (18.1 ppbv·h⁻¹) — showed
379 comparable or slightly higher $P(O_3)$ than our results. This comparison suggests that,
380 despite the moderate RO_2^* levels at our site, the instantaneous photochemical ozone
381 production remained considerably strong, pointing to an efficient RO_2^* –NO_x catalytic
382 cycle in Zhuhai.

383 Table 1. Summary of observed RO_2^* , HO₂, NO, O₃, and $P(O_3)$ during the field campaign.

Region	Location	Season, year	RO_2^* (pptv)	HO ₂ (pptv)	NO (ppbv)	O ₃ (ppbv)	$P(O_3)$ (ppbv/h)	References
Suburban	Paris, France	Summer, 2009	5.6	/	4	38	15.8 ^d	(Michoud et al., 2012)
Rural	Wangdu, China	Summer, 2014	43.23 ^a	19.52 ^a	0.72 ^a	72.37 ^a	10.44 ^{a,c}	(Tan et al., 2017)
Suburban	Heshan, China	Autumn, 2014	17.1	10.2	2.5	42.5	18.1 ^c	(Tan et al., 2019)
Urban	San Antonio, USA	Summer, 2017	37 ^b	/	0.23 ^b	40 ^b	4.2 ^{b,c}	(Anderson et al., 2019)
Urban	Guangzhou, China	Autumn, 2018	91.5	/	4.31	31.6	/	(Wang et al., 2023)
Suburban	Hefei, China	Summer, 2020	27.62	/	0.37	55.19	5.91 ^c	(Yu et al., 2023)
Suburban	Huabei, China	Autumn, 2021	50.34	/	0.3	52.66	19.5 ^d	(Wei et al., 2023)
Coastal	Zhuhai, China	Autumn, 2024	31.11	/	0.84	54.44	14.41 ^c	This work



384 Note: All unmarked data represent daytime averages (06:00–18:00).
385 ^a indicates daytime median values (06:00–16:00);
386 ^b indicates daytime median values (07:00–20:00);
387 ^c represents P(O₃) calculated based on the observed peroxy radical concentrations;
388 ^d represents P(O₃) calculated based on model-simulated peroxy radicals;
389 “/” represents data not available.

390

391 Based on our measurements, we can quantitatively distinguish the relative
392 contributions from local photochemical production and regional transport to surface O₃.
393 Considering the rapid equilibrium between NO₂ and O₃, the variation of odd oxidants
394 (d[Ox]/dt, where Ox = O₃ + NO₂) is used to reflect the combined influence of local
395 photochemical and transport on surface ozone. Therefore, the transport impact can be
396 expressed by R(O₃), which is calculated from the difference between d[Ox]/dt and
397 P(O₃)_{net} as defined in Eq. 8:

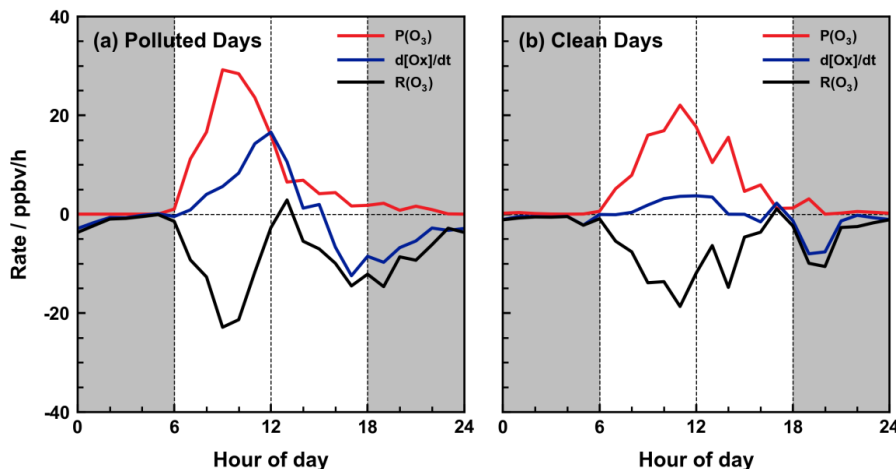
398
$$R(O_3) = \frac{dO_x}{dt} - P(O_3)_{net} \quad (Eq. 8)$$

399 Here, the sign of R(O₃) indicates the different influences from transport. When
400 R(O₃) > 0, regional transport enhances local O₃ concentrations, suggesting that O₃ could
401 be contributed by transport from surrounding regions. Conversely, R(O₃) < 0 implies
402 that transport acts as a dilution or export role in regulating the surface ozone.

403 The contribution from local photochemical production and transport to surface O₃
404 exhibited distinct patterns under different pollution conditions (Figure 6). We define the
405 polluted days as the maximum O₃ concentration exceeding the national Class I standard
406 of 160 µg/m³, while the clean periods corresponded to days with a maximum hourly O₃
407 concentration below 120 µg/m³. A total of 14 days and 4 days is categorized into
408 polluted and clean periods, respectively. The daytime increase in ozone concentration
409 in Zhuhai was primarily driven by local photochemical production, whereas regional
410 transport generally exhibited an export effect. However, the magnitudes and temporal
411 patterns of their contributions differed significantly between clean and pollution
412 scenarios. The P(O₃) exhibited similar diurnal variations among both polluted and clean
413 days, while polluted periods showed stronger ozone formation than clean periods.
414 Specifically, the peak P(O₃) on polluted days reached ~30 ppbv h⁻¹, which was
415 approximately 50% higher than that on clean days (~20 ppbv h⁻¹). In contrast to P(O₃),



416 the behavior of $R(O_3)$ on polluted days diverged significantly from that on clean days.
417 Around midday, $R(O_3)$ on polluted days rose rapidly from negative value to zero and
418 became slightly positive, indicating a suppressed airmass dispersion or even slight
419 import from regional O_3 . The distinct transport patterns during polluted days are
420 attributed to frequent coastal wind-field convergence that weakened ventilation. Such
421 weakening export in the midday facilitated the rapid accumulation of locally produced
422 ozone and contributed to the higher O_3 peaks during polluted days compared to clean
423 days. As a result, the elevated surface ozone on polluted days was resulted from the
424 combined effect of stronger photochemical production and reduced O_3 export in the
425 midday, whereas the $P(O_3)$ was almost offset by the transport effect of O_3 in clean days
426 leading to flat variation of O_3 .



427
428 Figure 6. Diurnal variations of $P(O_3)$, $d[Ox]/dt$, and $R(O_3)$ during (a) polluted and (b) clean periods.
429 The red line represents the photochemical ozone production rate $P(O_3)$, the blue line indicates the
430 rate of change of total oxidants $d[Ox]/dt$, and the black line corresponds to the regional transport
431 rate $R(O_3)$. The shaded areas (00:00–06:00 and 18:00–24:00) represent nighttime periods.
432

433 **4. Conclusions**

434 This study combined the PERCA technique with CEAS to develop a single-channel
435 PERCA–CEAS system. The system enables real-time, online measurements of RO_2^* ,
436 providing a robust technical support for evaluating atmospheric oxidation capacity and
437 elucidating tropospheric photochemical mechanisms. Experimental investigations were
438 conducted to determine key parameters affecting measurement performance. The



439 detection limit for RO₂* was 0.2 pptv (1 σ) at a time resolution of 3 min, with an overall
440 measurement uncertainty of 12–17%, demonstrating high sensitivity and stability that
441 meet the requirements for field observations of ambient RO₂*. Our PERCA–CEAS
442 system was successfully deployed for ambient measurement and found moderate RO₂*
443 levels in a coastal area. The P(O₃) derived from measured RO₂* is further used to
444 evaluate the O₃ formation regime and transport influence on O₃. The higher O₃ levels
445 observed on polluted days compared to clean days were driven by both stronger
446 photochemical production and reduced export effects during midday in this coastal area.
447 Our study, therefore, provides an important reference for extending the peroxy radical
448 measurement techniques to quantify in-situ formation and transport of O₃. We also
449 suggest more field observations of peroxy radicals in diverse environments to support
450 the strategy formulation of O₃ pollution.

451

452 **Data availability.** The dataset is available at

453 <https://doi.org/10.5281/zenodo.18346203> (Tang et al., 2026).

454 **Author Contributions Statement.** X.R.C. and H.C.W. conceived the study. R.J.T.,
455 and Z.L.Z., H.C.W. and X.R.C. analyzed the data and wrote the manuscript. R.J.T.,
456 Z.L.Z. set up the instrument and conducted the field experiment with the help of H.X.L.
457 and Y.M.W. All authors contributed to the results and commented on the manuscript.

458 **Competing Interests Statement.** The authors declare no competing interests.

459 **Acknowledgments.** H.C.W. received financial support from the National Key
460 Research and Development Program of China (2023YFC3710900), and the Guangdong
461 Natural Science Funds for Distinguished Young Scholar (2024B1515020075). X.R.C
462 received financial support from the National Natural Science Foundation of China (No.
463 22576242).

464

465 **References**

466 Anderson, D. C., Pavelec, J., Daube, C., Herndon, S. C., Knighton, W. B., Ler
467 ner, B. M., Roscioli, J. R., Yacovitch, T. I., and Wood, E. C.: Characterizati
468 on of ozone production in san antonio, texas, using measurements of total p
469 eroxy radicals, *Atmospheric Chem. Phys.*, 19, 2845–2860, <https://doi.org/10.5194/acp-19-2845-2019>, 2019.



471 Cantrell, C. A., Shetter, R. E., and Calvert, J.: Peroxy radical chemistry during
472 FIELDVOC 1993 in brittany, france, *Atmos. Environ.*, 30, 3947–3957, [https://doi.org/10.1016/1352-2310\(96\)00136-7](https://doi.org/10.1016/1352-2310(96)00136-7), 1996.

473 Chen, T., Zhang, P., Chu, B., Ma, Q., Ge, Y., Liu, J., and He, H.: Secondary
474 organic aerosol formation from mixed volatile organic compounds: effect of
475 RO₂ chemistry and precursor concentration, *Npj Clim. Atmospheric Sci.*, 5,
476 95–103, <https://doi.org/10.1038/s41612-022-00321-y>, 2022.

477 Chen, Y., Yang, C., Zhao, W., Fang, B., Xu, X., Gai, Y., Lin, X., Chen, W., a
478 nd Zhang, W.: Ultra-sensitive measurement of peroxy radicals by chemical a
479 mplification broadband cavity-enhanced spectroscopy, *Analyst*, 141, 5870–587
480 8, <https://doi.org/10.1039/C6AN01038E>, 2016.

481 Duncianu, M., Lahib, A., Tomas, A., Stevens, P. S., and Dusanter, S.: Characte
482 rization of a chemical amplifier for peroxy radical measurements in the atmo
483 sphere, *Atmos. Environ.*, 222, 117106, <https://doi.org/10.1016/j.atmosenv.2019.117106>, 2020.

484 Edwards, G. D., Cantrell, C. A., Stephens, S., Hill, B., Goyea, O., Shetter, R.
485 E., Mauldin, R. L., Kosciuch, E., Tanner, D. J., and Eisele, F. L.: Chemical
486 ionization mass spectrometer instrument for the measurement of tropospheric
487 HO₂ and RO₂, *Anal. Chem.*, 75, 5317–5327, <https://doi.org/10.1021/ac034402b>, 2003.

488 Ehn, M., Thornton, J. A., Kleist, E., Sipilä, M., Junninen, H., Pullinen, I., Spri
489 nger, M., Rubach, F., Tillmann, R., Lee, B., Lopez-Hilfiker, F., Andres, S.,
490 Acir, I.-H., Rissanen, M., Jokinen, T., Schobesberger, S., Kangasluoma, J., K
491 ontkanen, J., Nieminen, T., Kurtén, T., Nielsen, L. B., Jørgensen, S., Kjaerga
492 ard, H. G., Canagaratna, M., Maso, M. D., Berndt, T., Petäjä, T., Wahner,
493 A., Kerminen, V.-M., Kulmala, M., Worsnop, D. R., Wildt, J., and Mentel, T.
494 F.: A large source of low-volatility secondary organic aerosol, *Nature*, 506,
495 476–479, <https://doi.org/10.1038/nature13032>, 2014.

496 Gao, Y., Lu, K., and Zhang, Y.: Review of technologies and their applications
497 for the speciated detection of RO₂ radicals, *J. Environ. Sci.*, 123, 487–499,
498 <https://doi.org/10.1016/j.jes.2022.09.028>, 2023.

499 George, M., Andrés Hernández, M. D., Nenakhov, V., Liu, Y., and Burrows, J.
500 P.: Airborne measurement of peroxy radicals using chemical amplification co
501 upled with cavity ring-down spectroscopy: the PeRCEAS instrument, *Atmosp
502 heric Meas. Tech.*, 13, 2577–2600, <https://doi.org/10.5194/amt-13-2577-2020>, 2
503 020.

504 Green, T. J., Reeves, C. E., Brough, N., Edwards, G. D., Monks, P. S., and P
505 enkett, S. A.: Airborne measurements of peroxy radicals using the PERCA te
506 chnique, *J. Environ. Monit.*, 5, 75–83, <https://doi.org/10.1039/b204493e>, 2003.

507 Griffith, S. M., Hansen, R. F., Dusanter, S., Michoud, V., Gilman, J. B., Kuste
508 r, W. C., Veres, P. R., Graus, M., De Gouw, J. A., Roberts, J., Young, C.,
509 Washenfelder, R., Brown, S. S., Thalman, R., Waxman, E., Volkamer, R., Ts



513 ai, C., Stutz, J., Flynn, J. H., Grossberg, N., Lefer, B., Alvarez, S. L., Rapp
514 engueck, B., Mielke, L. H., Osthoff, H. D., and Stevens, P. S.: Measurements
515 of hydroxyl and hydroperoxy radicals during CalNex-LA: model comparisons
516 and radical budgets, *J. Geophys. Res. Atmospheres*, 121, 4211–4232, <https://doi.org/10.1002/2015JD024358>, 2016.

517

518 Hornbrook, R. S., Crawford, J. H., Edwards, G. D., Goyea, O., Mauldin III, R.
519 L., Olson, J. S., and Cantrell, C. A.: Measurements of tropospheric HO₂ and
520 RO₂ by oxygen dilution modulation and chemical ionization mass spectrometry,
521 *Atmospheric Meas. Tech.*, 4, 735–756, <https://doi.org/10.5194/amt-4-735-2011>, 2011.

522

523 Horstjann, M., Andrés Hernández, M. D., Nenakhov, V., Chrobry, A., and Burrows,
524 J. P.: Peroxy radical detection for airborne atmospheric measurements using
525 absorption spectroscopy of NO₂, *Atmospheric Meas. Tech.*, 7, 1245–1257,
526 <https://doi.org/10.5194/amt-7-1245-2014>, 2014.

527 Kartal, D., Andrés-Hernández, M. D., Reichert, L., Schlager, H., and Burrows,
528 J. P.: Technical note: characterisation of a DUALER instrument for the airborne
529 measurement of peroxy radicals during AMMA 2006, *Atmospheric Chem. Phys.*, 10,
530 3047–3062, <https://doi.org/10.5194/acp-10-3047-2010>, 2010.

531 Liang, W., Yu, H., Xu, H., Wang, Z., Li, T., Feng, Y., Russell, A., and Shi,
532 G.: Probing into ozone production through photochemistry of organic peroxy
533 radicals: implications for source control, *J. Geophys. Res. Atmospheres*, 129,
534 e2023JD040124, <https://doi.org/10.1029/2023JD040124>, 2024.

535 Liu, Y. and Zhang, J.: Atmospheric peroxy radical measurements using dual-channel
536 chemical amplification cavity ringdown spectroscopy, *Anal. Chem.*, 86,
537 5391–5398, <https://doi.org/10.1021/ac5004689>, 2014.

538 Lou, S., Tan, Z., Gan, G., Chen, J., Wang, H., Gao, Y., Huang, D., Huang, C.,
539 Li, X., Song, R., Wang, H., Wang, M., Wang, Q., Wu, Y., and Huang, C.:
540 Observation based study on atmospheric oxidation capacity in shanghai during
541 late-autumn: contribution from nitril chloride, *Atmos. Environ.*, 271, 11890
542 2, <https://doi.org/10.1016/j.atmosenv.2021.118902>, 2022.

543 Lu, K. D., Rohrer, F., Holland, F., Fuchs, H., Bohn, B., Brauers, T., Chang, C.
544 C., Häseler, R., Hu, M., Kita, K., Kondo, Y., Li, X., Lou, S. R., Nehr, S.,
545 Shao, M., Zeng, L. M., Wahner, A., Zhang, Y. H., and Hofzumahaus, A.: Observation
546 and modelling of OH and HO₂ concentrations in the pearl river delta 2006: a missing OH
547 source in a VOC rich atmosphere, *Atmospheric Chem. Phys.*, 12, 1541–1569,
548 <https://doi.org/10.5194/acp-12-1541-2012>, 2012.

549 Ma, X., Tan, Z., Lu, K., Yang, X., Liu, Y., Li, S., Li, X., Chen, S., Novelli,
550 A., Cho, C., Zeng, L., Wahner, A., and Zhang, Y.: Winter photochemistry in
551 beijing: observation and model simulation of OH and HO₂ radicals at an urban
552 site, *Sci. Total Environ.*, 685, 85–95, <https://doi.org/10.1016/j.scitotenv.2019.05.329>, 2019.



554 Ma, X., Tan, Z., Lu, K., Yang, X., Chen, X., Wang, H., Chen, S., Fang, X.,
555 Li, S., Li, X., Liu, J., Liu, Y., Lou, S., Qiu, W., Wang, H., Zeng, L., and Z
556 hang, Y.: OH and HO₂ radical chemistry at a suburban site during the EXP
557 LORE-YRD campaign in 2018, *Atmospheric Chem. Phys.*, 22, 7005–7028, ht
558 tps://doi.org/10.5194/acp-22-7005-2022, 2022.

559 Michoud, V., Kukui, A., Camredon, M., Colomb, A., Borbon, A., Miet, K., Au
560 mont, B., Beekmann, M., Durand-Jolibois, R., Perrier, S., Zapf, P., Siour, G.,
561 Ait-Helal, W., Locoge, N., Sauvage, S., Afif, C., Gros, V., Furger, M., Anc
562 ellet, G., and Doussin, J. F.: Radical budget analysis in a suburban european
563 site during the MEGAPOLI summer field campaign, *Atmospheric Chem. Ph*
564 ys., 12, 11951–11974, https://doi.org/10.5194/acp-12-11951-2012, 2012.

565 Mihelcic, D., Müsgen, P., and Ehhalt, D. H.: An improved method of measurin
566 g tropospheric NO₂ and RO₂ by matrix isolation and electron spin resonanc
567 e, *J. Atmospheric Chem.*, 3, 341–361, https://doi.org/10.1007/BF00122523, 19
568 85.

569 Mihelcic, D., Volz-Thomas, A., Pätz, H. W., Kley, D., and Mihelcic, M.: Num
570 erical analysis of ESR spectra from atmospheric samples, *J. Atmospheric Ch*
571 em., 11, 271–297, https://doi.org/10.1007/BF00118353, 1990.

572 Mihele, C. M., Mozurkewich, M., and Hastie, D. R.: Radical loss in a chain r
573 eaction of CO and NO in the presence of water: implications for the radical
574 amplifier and atmospheric chemistry, *Int. J. Chem. Kinet.*, 31, 145–152, ht
575 ps://doi.org/10.1002/(SICI)1097-4601(1999)31:2%253C145::AID-KIN7%253E3.0.
576 CO;2-M, 1999.

577 Monks, P. S.: Gas-phase radical chemistry in the troposphere, *Chem. Soc. Rev.*,
578 34, 376, https://doi.org/10.1039/b307982c, 2005.

579 Orlando, J. J. and Tyndall, G. S.: Laboratory studies of organic peroxy radical
580 chemistry: an overview with emphasis on recent issues of atmospheric signifi
581 cance, *Chem. Soc. Rev.*, 41, 6294, https://doi.org/10.1039/c2cs35166h, 2012.

582 Reichert, L., Andrés Hernández, M. D., Stöbener, D., Burkert, J., and Burrows,
583 J. P.: Investigation of the effect of water complexes in the determination of
584 peroxy radical ambient concentrations: implications for the atmosphere, *J. G*
585 eophys. Res. Atmospheres, 108, https://doi.org/10.1029/2002JD002152, 2003.

586 Sommariva, R., Brown, S. S., Roberts, J. M., Brookes, D. M., Parker, A. E.,
587 Monks, P. S., Bates, T. S., Bon, D., De Gouw, J. A., Frost, G. J., Gilman,
588 J. B., Goldan, P. D., Herndon, S. C., Kuster, W. C., Lerner, B. M., Osthoff,
589 H. D., Tucker, S. C., Warneke, C., Williams, E. J., and Zahniser, M. S.: Oz
590 one production in remote oceanic and industrial areas derived from ship base
591 d measurements of peroxy radicals during TexAQS 2006, https://doi.org/10.51
592 94/acpd-10-23109-2010, 7 October 2010.

593 Tan, Z., Fuchs, H., Lu, K., Hofzumahaus, A., Bohn, B., Broch, S., Dong, H.,
594 Gomm, S., Häseler, R., He, L., Holland, F., Li, X., Liu, Y., Lu, S., Rohrer,
595 F., Shao, M., Wang, B., Wang, M., Wu, Y., Zeng, L., Zhang, Y., Wahner,



596 A., and Zhang, Y.: Radical chemistry at a rural site (wangdu) in the north
597 China plain: observation and model calculations of OH, HO₂ and RO₂ radica
598 ls, *Atmospheric Chem. Phys.*, 17, 663–690, <https://doi.org/10.5194/acp-17-663-2017>, 2017.

600 Tan, Z., Lu, K., Dong, H., Hu, M., Li, X., Liu, Y., Lu, S., Shao, M., Su, R.,
601 Wang, H., Wu, Y., Wahner, A., and Zhang, Y.: Explicit diagnosis of the loca
602 l ozone production rate and the ozone-NO_x-VOC sensitivities, *Sci. Bull.*, 63,
603 1067–1076, <https://doi.org/10.1016/j.scib.2018.07.001>, 2018a.

604 Tan, Z., Rohrer, F., Lu, K., Ma, X., Bohn, B., Broch, S., Dong, H., Fuchs, H.,
605 Gkatzelis, G. I., Hofzumahaus, A., Holland, F., Li, X., Liu, Y., Liu, Y., No
606 velli, A., Shao, M., Wang, H., Wu, Y., Zeng, L., Hu, M., Kiendler-Scharr,
607 A., Wahner, A., and Zhang, Y.: Wintertime photochemistry in beijing: observ
608 ations of RO_x radical concentrations in the north China plain during the B
609 EST-ONE campaign, *Atmospheric Chem. Phys.*, 18, 12391–12411, <https://doi.org/10.5194/acp-18-12391-2018>, 2018b.

610 Tan, Z., Lu, K., Hofzumahaus, A., Fuchs, H., Bohn, B., Holland, F., Liu, Y.,
611 Rohrer, F., Shao, M., Sun, K., Wu, Y., Zeng, L., Zhang, Y., Zou, Q., Kiendl
612 er-Scharr, A., Wahner, A., and Zhang, Y.: Experimental budgets of OH, HO₂,
613 and RO₂ radicals and implications for ozone formation in the pearl river de
614 lta in China 2014, *Atmospheric Chem. Phys.*, 19, 7129–7150, <https://doi.org/10.5194/acp-19-7129-2019>, 2019.

615 Tan, Z., Ma, X., Lu, K., Jiang, M., Zou, Q., Wang, H., Zeng, L., and Zhang,
616 Y.: Direct evidence of local photochemical production driven ozone episode i
617 n beijing: a case study, *Sci. Total Environ.*, 800, 148868, <https://doi.org/10.1016/j.scitotenv.2021.148868>, 2021.

618 Tang, R., Zheng, Z., and Chen, X.: Measurement report: development of a port
619 able peroxy radical measurement system, <https://doi.org/10.5281/ZENODO.18346203>, 2026.

620 Thornton, J. A., Wooldridge, P. J., Cohen, R. C., Martinez, M., Harder, H., Br
621 une, W. H., Williams, E. J., Roberts, J. M., Fehsenfeld, F. C., Hall, S. R., S
622 heter, R. E., Wert, B. P., and Fried, A.: Ozone production rates as a functio
623 n of NO_x abundances and HO_x production rates in the nashville urban plum
624 e, *J. Geophys. Res. Atmospheres*, 107, <https://doi.org/10.1029/2001JD000932>,
625 2002.

626 Wang, H., Liu, Y., Chen, X., Gao, Y., Qiu, W., Jing, S., Wang, Q., Lou, S., E
627 dwards, P. M., Huang, C., and Lu, K.: Unexpected fast radical production e
628 merges in cool seasons: implications for ozone pollution control, *Natl. Sci.*
629 *Open*, 1, 20220013, <https://doi.org/10.1360/ns0/20220013>, 2022.

630 Wang, J., Zhang, Y., Zhao, W., Wu, Z., Luo, S., Zhang, H., Zhou, H., Song,
631 W., Zhang, W., and Wang, X.: Observationally constrained modeling of pero
632 xy radical during an ozone episode in the pearl river delta region, china, J.

633



637 Geophys. Res. Atmospheres, 128, e2022JD038279, <https://doi.org/10.1029/2022JD038279>, 2023.

638 Wei, N., Zhao, W., Yao, Y., Wang, H., Liu, Z., Xu, X., Rahman, M., Zhang, C., Fittschen, C., and Zhang, W.: Peroxy radical chemistry during ozone photochemical pollution season at a suburban site in the boundary of jiangsu–an hui–shandong–henan region, China, *Sci. Total Environ.*, 904, 166355, <https://doi.org/10.1016/j.scitotenv.2023.166355>, 2023.

639 Whalley, L. K., Blitz, M. A., Desservettaz, M., Seakins, P. W., and Heard, D. E.: Reporting the sensitivity of laser-induced fluorescence instruments used for HO₂ detection to an interference from RO₂ radicals and introducing a novel approach that enables HO₂ and certain RO₂ types to be selectively measured, *Atmospheric Meas. Tech.*, 6, 3425–3440, <https://doi.org/10.5194/amt-6-3425-2013>, 2013.

640 Wood, E. C. and Charest, J. R.: Chemical amplification - cavity attenuated phase shift spectroscopy measurements of atmospheric peroxy radicals, *Anal. Chem.*, 86, 10266–10273, <https://doi.org/10.1021/ac502451m>, 2014.

641 Yang, C., Zhao, W., Fang, B., Yu, H., Xu, X., Zhang, Y., Gai, Y., Zhang, W., Chen, W., and Fittschen, C.: Improved chemical amplification instrument by using a nafion dryer as an amplification reactor for quantifying atmospheric peroxy radicals under ambient conditions, *Anal. Chem.*, 91, 776–779, <https://doi.org/10.1021/acs.analchem.8b04907>, 2019.

642 Yang, X., Lu, K., Ma, X., Gao, Y., Tan, Z., Wang, H., Chen, X., Li, X., Huang, X., He, L., Tang, M., Zhu, B., Chen, S., Dong, H., Zeng, L., and Zhang, Y.: Radical chemistry in the pearl river delta: observations and modeling of OH and HO₂ radicals in shenzhen in 2018, *Atmospheric Chem. Phys.*, 22, 12525–12542, <https://doi.org/10.5194/acp-22-12525-2022>, 2022.

643 Yu, H., Wei, N. N., Xu, X. Z., Liu, Q. Q., Yao, Y. C., Zhao, W. X., and Zhang, W. J.: Characteristics of Summer O₃ Formation in the Western Suburbs of Hefei Based on Total Peroxy Radical Observations, *Environ. Sci.*, 44, 1974–1984, <https://doi.org/10.13227/j.hjkx.202206116>, 2023 (in Chinese).

644 Zhang, G., Hu, R., Xie, P., Hu, C., Liu, X., Zhong, L., Cai, H., Zhu, B., Xia, S., Huang, X., Li, X., and Liu, W.: Intensive photochemical oxidation in the marine atmosphere: evidence from direct radical measurements, <https://doi.org/10.5194/egusphere-2023-550>, 19 June 2023.

645 Zheng, Z., Wang, H., Chen, X., Wang, J., Li, X., Lu, K., Yu, G.-H., Huang, X., and Fan, S.: A mini broadband cavity enhanced absorption spectrometer for nitrogen dioxide measurement on the unmanned aerial vehicle platform, *Atmos. Environ.*, 321, 120361, <https://doi.org/10.1016/j.atmosenv.2024.120361>, 2024.

646 Zou, Z., Chen, T., Chen, Q., Sun, W., Han, S., Ren, Z., Li, X., Song, W., Ge, A., Wang, Q., Tian, X., Pei, C., Wang, X., Zhang, Y., and Wang, T.: Observation and modeling of atmospheric OH and HO₂^{*} radicals at a subtropical r



679 ural site and implications for secondary pollutants, Atmospheric Chem. Phys.,
680 25, 8147–8161, <https://doi.org/10.5194/acp-25-8147-2025>, 2025.
681